Sharp Volcano-Type Synergy and Visible Light Acceleration in H 2 Release upon B 2 (OH) 4 Hydrolysis Catalyzed by Au-Rh@Click-Dendrimer Nanozymes

Qiuxia Zhao, Naixin Kang, Marta Martinez Moro, Eduardo Guisasola Cal, Sergio Moya, Emerson Coy, Lionel Salmon, Xiang Liu, Didier Astruc

Sharp Volcano-Type Synergy and Visible-Light Acceleration in H_2 Release upon $B_2(OH)_4$ Hydrolysis Catalyzed by Au-Rh@click-dendrimer Nanozymes

Qiuxia Zhao, Naixin Kang, Marta Martinez Moro, Eduardo Guisasola Cal, Sergio Moya, Emerson Coy, Lionel Salmon, Xiang Liu, Didier Astruc,*

Abstract

Hydrogen (H_2) formation from hydrogen-rich precursors is a hot topic, whereby carbon-free energy perspectives, mechanistic features and synthetic applications are actively searched. Here, we report oxygen atom uptake from water under ambient conditions producing H_2 in the presence of alloyed Au-Rh nanoparticle (NP) catalysts encapsulated in a "click" dendrimer. These systems are named nanozymes (NZs), because their function and mechanism resemble that of hydrogenase enzymes. The Au-Rh NZs with variable proportions of Au and Rh exhibit positive sharp volcano-type synergy and visible-light induced acceleration. The best synergy in the dark is disclosed in Au_4Rh_1, achieving a turnover frequency (TOF_s) of 5100 mol_{H_2} mol_{cata}^{-1} min^{-1} in dark, 3.4 times higher than related Au NZ and 8.9 times higher than the related Rh NZ at 25 ± 1 °C. The catalytic activity of Au-Rh for H_2 evolution is enhanced by visible-light irradiation due to the Au plasmon, so that the synergistic effect in the dark and the visible-light induced rate enhancement cumulate for Au_4Rh_1, allowing complete $B_2(OH)_4$ hydrolysis in 39 sec at 25 ± 1°C (TOF_s = 6000 mol_{H_2} mol_{cata}^{-1} min^{-1}). Upon increasing the Rh content, Au-Rh provides less synergy in the dark, whereas the light enhancement of the reaction rate increases, reaching a maximum for Au_1Rh_2. Experiments using D_2O, including kinetic isotope effect determination, suggest that the rate-determining step of the reaction involves concerted O-H bond cleavage of water and support the proposed catalytic reaction mechanism.

Keywords: hydrogen production; $B_2(OH)_4$ hydrolysis; plasmonic rate enhancement; volcano-synergy effect; visible-light acceleration; gold; rhodium

1. Introduction

We report oxygen atom uptake from H_2O producing H_2 upon reaction with $B_2(OH)_4$ catalyzed under ambient condition by bimetallic Au-Rh nano-particles (NPs) encapsulated in a "click"-dendrimer. These nano catalysts of metallo-macromolecular type play the role of "nanozymes" (NZs), a general term currently utilized for artificial nanomaterials with catalytic activities resembling those of enzymes. [1] In the present case, we will show some resemblance of these nanocatalysts [2] with hydrogenase that catalyze the formation of H_2 from water protons, including mechanistic results. [3,4] $B_2(OH)_4$, a useful borylation agent, sometimes used in hydrogenation reactions, [5-8] is potentially usable for H_2 generation upon hydrolysis according to equation (1):

$$B_2(OH)_4 + 2\,H_2O \rightarrow 2\,B(OH)_3 + H_2\uparrow \quad (1)$$

Transfer hydrogenation [9] of unsaturated hydrocarbon using catalytic $B_2(OH)_4$ hydrolysis was pioneered in 2016 by Stokes and his group who reported that this reaction could be used for hydrogenation and deuteration of a variety of alkenes and alkynes and showed that both hydrogen atoms of water were transferred to the unsaturated substrates. [5] A catalytic mechanism was suggested without H_2 formation involving the intermediacy of a Pd-H species in which the unsaturated hydrocarbon inserted to end up with its hydrogenation. It has also been shown that H_2 formation proceeded upon Pd-catalyzed hydrolysis of $B_2(OH)_4$. [9] For comparison, ammonia borane (AB) hydrolysis is a well-known classic method of H_2 generation in which one of the generated H_2 atoms (the "hydridic" one) is provided by hydrogen-rich AB and the other one (the "acidic" one) from water. [10] On the other hand, $B_2(OH)_4$ only contains acidic hydrogen atoms, and apparently both hydrogen atoms of produced H_2 seem to come from water (*vide infra*), thus none would come from $B_2(OH)_4$. Consequently, $B_2(OH)_4$ is not a hydrogen storage material, contrary to AB and derivatives. By the way, the fact that water behaves as a hydrogen storage source upon utilizing $B_2(OH)_4$ hydrolysis offers a D_2 production method from D_2O, applicable for the deuteration of unsaturated compounds of extensive utility in mechanism studies, [11] and analytical chemistry. [12,13]

$B_2(OH)_4$ is stable in water at room temperature, and thus a catalyst is required for its hydrolysis to H_2 according to equation (1). Formation of H_2 would be of interest given the considerable application in its production as a long-term sustainable energy supply. [14-19]

Given the absence of reasonably practical loop to recycle $B_2(OH)_4$ from the reaction product $B(OH)_3$, however, reaction (1) can rather be considered as a test reaction and a useful and fast way to produce H_2 or D_2 on the laboratory scale under ambient conditions. Bimetallic NPs, constituted of two distinct metal elements, often show an enhanced chemical performance compared to those of their monometallic counterparts.[20] The presence of a second metal indeed usually provokes a modification of the electronic state of each metal in the NP and consequently modifies the catalytic activity of the bimetallic nanocatalysts. Besides, the second metal induces a geometric effect often reducing the number of multiple adsorption sites by partially blocking the surface or facilitating access to more active sites owing to specific atomic arrangement. [21] This frequently positive synergistic effect has received much attention in optical, catalytic, and photocatalytic applications. [20]

Photocatalysis is regarded as a prominent approach utilizing the endless and diffuse solar energy. [22] ~~Recently,~~ the plasmonic metal NPs (PMNPs) [23] have drawn much attention owing to their surface plasmonic resonant (SPR) effect that is utilized for plasmonic photocatalytic hydrogen evolution. Light excitation provokes hot charge transfer to the nearby substrate for a few tenths of fs, which reduces the activation energy of the reaction of the adsorbed substrate. [24] Therefore, PMNP morphology, size and structure control the efficiency of the photocatalytic system. [25,26]

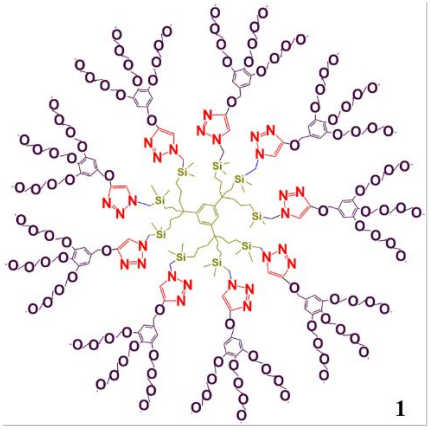

Figure 1. "Click" dendrimer **1**.

Dendrimer-RNA NPs are known to provide protective immunity against several lethal viruses, [27] and polyamidoamine (PAMAM) dendrimers encapsulating NPs have functioned as catalysts. [28,29] Dendrimers of "click" type are known as effective nanocatalyst encapsulating supports for a variety of reactions. [30] They contain intradendritic 1,2,3-triazolyl groups resulting from "click" reactions. They are therefore called "click" dendrimers (Figure 1), because they result from the Cu(I)-catalyzed Huisgen 1,3-dipolar azide-alkyne cycloaddition (CuAAC, the most known so-called "click" reaction [31]) of the terminal azido groups of dendrimer cores with dendrons containing an alkyne group at their focal points. These "click" dendrimers, such as **1**, are of micellar type, due to their hydrophobic interior and the presence of hydrophilic triethylene glycol (TEG) terminal groups. They are dendritic amphiphilic unimolecular micelles allowing coordination, to their intradendritic triazole groups, of transition-metal ions and, more mildly, NPs. [31] These intradendritically coordi-nated metal cations and NPs are stabilized by protection, due to the bulk of the "click" dendrimer periphery. Therefore, here, "click"-dendrimer-encapsulated, mono-metallic and bimetallic transition metal NPs including Au have been prepared, tested and compared towards H_2 evolution upon $B_2(OH)_4$ hydrolysis under both dark and visible-light illumination conditions. Several gold-containing bimetallic nano-catalytic systems, Au_x-Rh_y have been selected and examined with various metal ratios, allowing to determine the optimized metal ratios in the dark, light-induced acceleration, and combined effects. From these results, the benefits of bimetallic synergy and visible light illumination are analyzed and discussed. Finally, hydrolysis experiments using D_2O instead of H_2O including determination of the kinetic isotope effect (KIE) are carried out in order to contribute to a mechanistic proposal concerning the AuRh NZ-catalyzed $B_2(OH)_4$ hydrolysis.

2. Experimental Section

2.1. Materials

The precursors used for the click-dendrimer-encapsulated NP preparations, $RhCl_3$, $KAuCl_4 \cdot xH_2O$, $NaBH_4$ and $B_2(OH)_4$ were purchased from Sigma-Aldrich and are analytical grade. All flasks were washed with aqua regia (HCl: HNO_3 = 3:1) before usage to avoid the presence of metal residues. Milli-Q water (18.2 MΩ, Thermo Fischer Scientific Inc., USA) was used in the process of NP fabrication and catalytic reactions.

2.2. Synthesis of the "click" dendrimer-encapsulated Au-Rh NZs

The "click" dendrimer (Figure 1 and S1) containing nine 1,2,3-triazole ligands on the tethers and 27 water-solubilizing triethylene glycol termini was fabricated via a method previously reported. [32] Taking advantage of the presence of nitrogen-rich 1,2,3-triazoles along the "click" dendrimer tethers, Rh (III) and Au (III) were coordinated to the intra-dendritic 1,2,3-triazoles upon blending together their precursor metal derivatives with the dendrimer under N_2. Then, the Au-Rh NPs were generated upon addition of a freshly-prepared solution of the reductant $NaBH_4$ to the dendrimer-metal (III) assembly (Scheme 1). [33] The composition of Au and Rh in the bimetallic NPs is termed as Au_xRh_y, where x and y indicate the molar ratio of Au and Rh, for example Au_4Rh_1 for an Au-Rh NZ containing 80% mol Au and 20% mol Rh. Various Au_xRh_y NPs were prepared upon varying the proportions x/y of the metal precursors from 0.5 to 6.

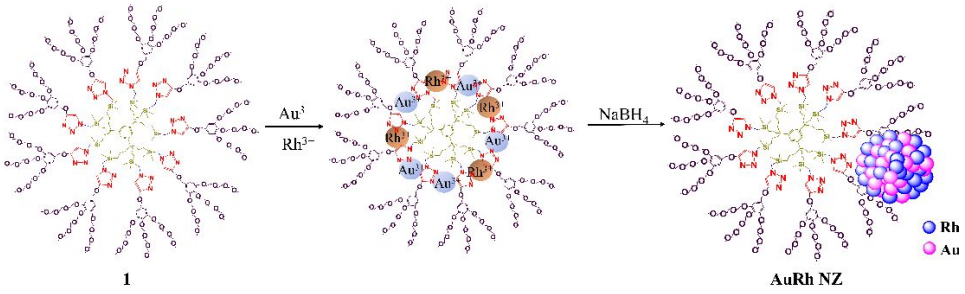

Scheme 1. Synthesis of various Au-Rh NZs supported by the "click" dendrimer **1**.

2.3. Au-Rh NZ characterizations

The overall characterizations of the Au-Rh @click-dendrimer NZs were carried

out using NMR and UV-vis. spectroscopies, transmission electron microscopy (TEM), high-resolution TEM (HRTEM), Energy-Dispersive X-ray Spectroscopy (EDS), X-ray Photoelectron Spectroscopy (XPS) and chromatography-mass spectrometry (GC-MS). Bruker AC 300 MHz was used for the NMR spectra with all chemical shifts in parts per million (δ, ppm) referring to TMS at room temperature. UV- vis. spectra were recorded using a Perkin-Elmer Lambda 19 UV-vis. spectrometer. TEM images were recorded on TEM JEOL JEM 1400 (120 kV) - 2100F. HRTEM images were recorded by Jéol JEM-ARM200f -200 kV with a probe corrector, which was also equipped with a STEM HAADF system (Scanning Transmission Electron Microscopy Hight Angle Annular Dark Field) and energy-dispersive X-ray Spectroscopy (EDS) analysis system. XPS experiments were performed in a SPECS Sage HR 100 spectrometer with a non-monochromatic X-ray source (magnesium Kα line of 1253.6 eV energy and 252 W)

2.4. Catalytic reactions

The catalytic hydrolysis of $B_2(OH)_4$ was carried out at 25 ± 1 °C. In a typical experiment, 0.1 % mmol Au-Rh NZ dissolved in 4 ml deionized water was placed in a 50-ml round bottom flask with two outlets. Then, $B_2(OH)_4$ (1mmol, 90 mg) dissolved in 5 ml deionized water was added under vigorous stirring. The measurement of the produced H_2 gas was conducted in a typical water-filled gas burette. A 7-W visible LED lamp (Sunshine Lighting Limited, France) with a light intensity of 1540 lx was used for the light irradiation. The temperature of the reaction was measured using an electronic thermometer.

3. Results and discussions

3.1. Au-Rh NZ characterizations

The microstructure and size distribution of the metal NPs were investigated by TEM and high-resolution TEM (HRTEM). The as-prepared mono- and bimetallic NPs are homogeneously dispersed with a narrow small size distribution (Figure 2 and S2-S14). For Au_4Rh_1 NPs, a very fine diameter size distribution of 1.5 ± 0.4 nm is observed (Figure S4). This good confinement of the NPs is attributed to the stabilization effect of the intradendritic triazole ligands that coordinate to the gold and rhodium atoms. The intra-dendritic NPs make these nano-assemblies resemble metalloenzymes in their sizes, inner

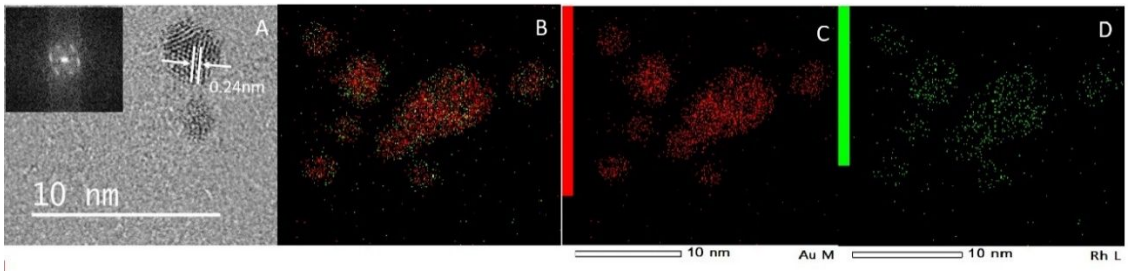

Figure 2. Transmission Electron Microscopy for Au_4Rh_1 NZs. HRTEM images; inset: corresponding Fast-Fourier transform (FFT) pattern (A). EDX elemental mapping images of the overlapped Au and Rh (B), and Au mapping (C) and Rh mapping (D)

catalytic site localization, transition-metal catalysts and hydrogenase-like function (*vide infra,* mechanistic section). [3, 28] Figure 2A exhibits clear lattice fringes with a space of 0.24 nm, which confirms the crystallinity of the Au_4Rh_1 NPs. A diffraction pattern with six-fold rotational symmetry in the inset fast-Fourier transform pattern evidences the (111) facets of Au and Rh. [34] The element mapping of Au and Rh by EDS) (Figure 2B, 2C, 2D) shows the alloy structure of the Au_4Rh_1 NZ. The Au element is more concentrated in the core of the NPs, which is also evidenced by the distribution of Au and Rh along the cross-section (Figure S9).

In order to investigate the surface electronic structure, XPS was recorded for the dendritic and the Au-Rh alloy NZ parts. As shown in Figure 3, comparing to the binding energy of pure AuNPs (87.38 eV and 83.70 eV) and pure RhNPs (312.63 eV and 307.96 eV), the alloyed Au_4Rh_1NZs exhibits a small upshift of 0.14 and 0.16 eV for Au^0 and a large upshift of 2.02 and 2.25 eV for Rh^0. The XPS data show that the Au atoms are not

much perturbed upon alloying, whereas the Rh 3d orbitals are shifted to higher energy upon alloying Rh with Au, which means that the Rh atoms undergo some decrease of electron density in the Au-Rh alloy upon atom redistribution. [35,36]

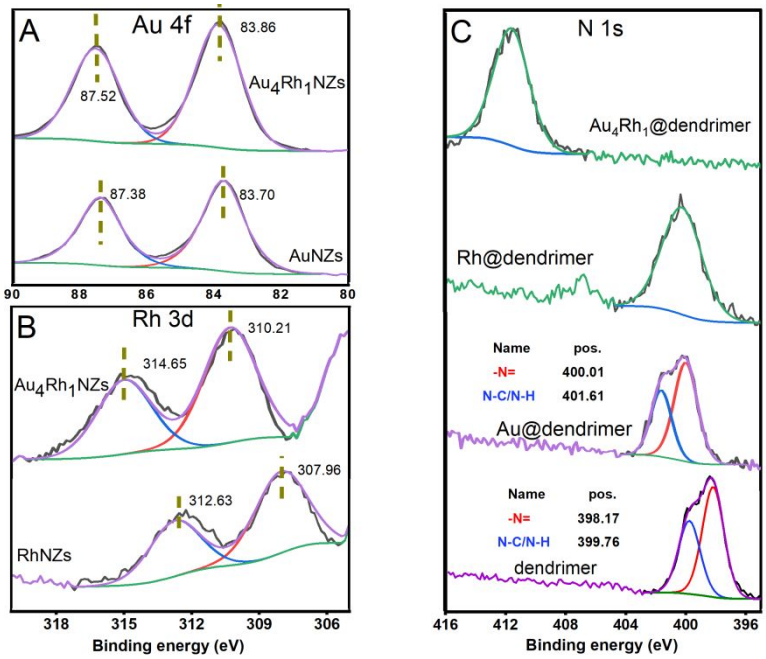

Figure 3. XPS patterns of the Au 4f (A), Rh 3d (B) for AuNZs, RhNZs, Au_4Rh_1NZs and N 1s for dendrimer, RhNPs@dendrimer, AuNPs@dendrimer and Au_4Rh_1NPs @dendrimer.

Let us now examine the shifts occurring for the dendritic triazole N 1s band upon dendrimer coordination to the alloyed metal atoms. The N 1s region of the dendrimer has two components centered at 398.17 and 399.76 eV that are assigned to -N=C- and -N-C/N-H of the triazole ligand in the dendrimer (Figure 3). [37,38] After loading the metal NPs in the dendrimer, the N 1s bands shift towards higher binding energies, exhibiting peaks at 400.01eV and 401.61eV for the monometallic AuNPs, 400.27eV for the monometallic RhNPs and 411.56 eV for the Au_4Rh_1NPs, which discloses significant electronic interactions between the NPs and the triazole ligand. The significance of the higher binding energy values in the NZ compared to the dendrimer alone is a decreased electron density on the dendritic N atoms upon coordination to the metals due to the N ligand electronic donation to these metal atoms.

Let us now consider the reduction by $NaBH_4$ of the two intra-dendritically coordinated metal cations to metal (0) NPs. Au^{3+} has a higher reduction potential than Rh^{3+} and, based on this consideration only, the Marcus theory region for exergonic electron transfer would

dictate faster Au NP formation compared to Rh NP formation. [39] The coordination of chlorides and heteroatom ligands of the dendrimer, including in particular triazoles, changes the reduction potentials of the metal cations, however. Then, another factor that affects the relative rates of formation of the two NPs is the nucleation kinetics. Altogether, there is still a preference for the faster Au NP formation compared to the Rh NP formation, and the result may then be either formation of an Au@Rh core-shell NP or an alloy with an Au-enriched core. For instance, a related case was reported by Tsang's group with Ag@Pd NPs that catalyzed H_2 production from formic acid. [40] From EDX data obtained through the cross-section line element mapping (Figure S9 and S10), it is concluded that the alloy structure preferably contains Rh atoms located at the periphery of these bimetallic NPs and preferably Au atoms at the center. When the Au proportion is dominant, however, the introduction of a small amount of Rh is envisioned to tune the electron distribution of Au and Rh and generate defect sites at the surface of the Au-Rh NPs. [34]

3.2. Volcano-type synergistic effects in Au-Rh nanozymes for $B_2(OH)_4$ hydrolysis

A series of "click" dendrimer-supported Au_xRh_y NPs with diverse Au and Rh proportions (Rh mole content varying from 0 to 100%) were applied as NZs for the hydrolysis of $B_2(OH)_4$ at 25 ± 1 °C. The time profile plots of H_2 evolution and TOF_s values of Au-Rh nanozyme-catalyzed $B_2(OH)_4$ hydrolysis are presented in Figure 4. The catalytic performance of H_2 evolution is determined by the reaction time at 10% $B_2(OH)_4$ conversion. Thus, the TOF_s value here is defined as mole of generated H_2 divided by the total number of surface atoms over the time span of 10% $B_2(OH)_4$ conversion. [41] When 1 mmol $B_2(OH)_4$ is consumed, 1 equiv. H_2 is produced in $B_2(OH)_4$ hydrolysis (Equation (1)). The monometallic Au and Rh NZs are valuable catalysts providing TOF_s values of 1500 and 570 mol_{H_2} mol_{cata}^{-1} min^{-1} (Table 1), respectively, which indicates that the Au NZ is more active than Rh NZ. This result is opposite to those reported for NPs supported by graphene quantum dots (GQDs) reported by Jang *et al*, demonstrating a dramatic effect of the support on the nanocatalysts. [9] However, a dramatic rise of the TOF_s value was observed when Rh was introduced to form Au-Rh NZs. As shown in Figure 4B, the alloyed Au-Rh NZs displayed an enhanced catalytic activity compared to the monometallic counterparts, with

a TOF_s value of 3700 mol_{H_2} mol_{cata}^{-1} min^{-1} for Au_6Rh_1, 5100 mol_{H_2} mol_{cata}^{-1} min^{-1} for Au_4Rh_1, 3200 mol_{H_2} mol_{cata}^{-1} min^{-1} for Au_2Rh_1, and 1900 mol_{H_2} mol_{cata}^{-1} min^{-1} for Au_1Rh_2, respectively (Table 1).

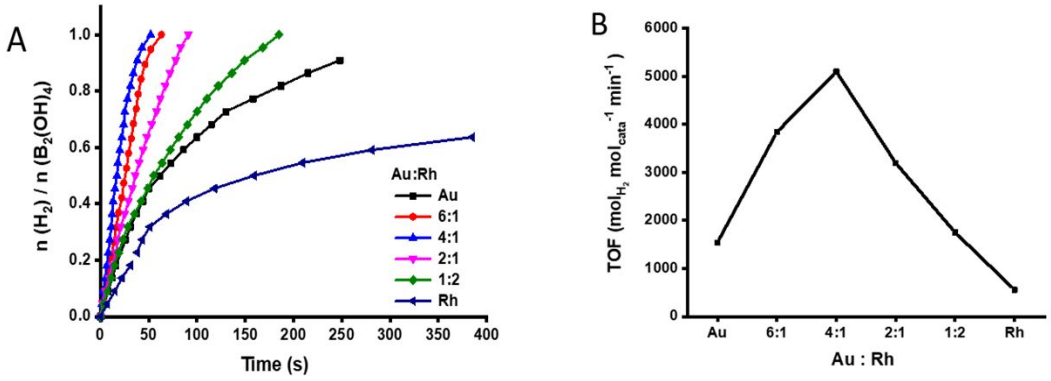

Figure 4. (A) Time profile plots of H_2 evolution and (B) TOF_s value of $B_2(OH)_4$ hydrolysis catalyzed by 0.1 mol % Au-Rh NZs with different Au/Rh molar ratios in the dark at 25± 1 ˚C

Among all the NZs, Au_4Rh_1 NZ exhibited the highest enhancement with a 3.4-time higher TOF_s value compared to pristine Au NZ under the same conditions. All these results reveal an impressive volcano-type synergistic effect between the Au and Rh components. To verify the bimetallic synergy between Au and Rh, a mixture of 80% monometallic Au NZ and 20% monometallic Rh NZ was conducted for $B_2(OH)_4$ hydrolysis, and the result (Figure S 17A) indicates that there is no additional efficiency upon physically blending these two monometallic NZs. Besides, the recyclability of the best Au_4Rh_1NZ shows completion of quantitative hydrolysis during 4 cycles in dark, requiring progressively increased reaction time along these cycles, however (Figure 5A). There is slightly reduced efficiency of this NZ catalyst upon recycling. Catalytic AuRh NZ efficiency is demonstrated upon $B_2(OH)_4$ hydrolysis in the absence of catalyst (Figure S20) at 25˚C, 50˚C and 90˚C, which indicates that catalysis at 25˚C even with Au_1Rh_2 NZ that shows the least synergy is faster than $B_2(OH)_4$ hydrolysis alone at 90˚C. It is known that the substrate adsorption and product desorption step impact the efficiency of the catalyst. [34,42] When Au alloys with Rh, tuning the Au and Rh composition, Au_4Rh_1NZ and Au_1Rh_2NZ exhibit different Rh exposures of NP surfaces (Figure 2, Figure S8), which results in a diversity of active sites, and thus different catalytic performances. Additionally, electronic effects also

Table 1 TOF values of Au-Rh NZ catalysts with various molar ratios under dark and light conditions at 25 ±1 ºC unless noted otherwise.

catalyst	Au_1Rh_0	Au_6Rh_1	Au_4Rh_1	Au_2Rh_1	Au_1Rh_2	Au_1Rh_2 28±1°C	Au_0Rh_1
Time(s)-dark	248±5	63±2	52±2	91±2	185±2	153±2	385±8
TOF_t-dark	410±30	1200±80	1800±180	820±40	530±20	2000±200	132±4
TOF_s-dark	1500±100	3700±300	5100±400	3200±300	1900±300	5700±400	570±70
Time (s)-light	237±5	52±2	39±2	69±2	131±2	-	379±8
TOF_t-light	410±40	1300±150	2100±400	1100±100	735±50	-	134±4
TOF_s-light	1500±500	4000±300	6000±400	4300±300	2600±500	-	580±70
R_{atom}(nm)	0.135	0.135	0.135	0.135	0.135	-	0.135
R_L/R_D	1.0	1.1	1.2	1.3	1.4		1.0
Size(nm)	2.0±0.4	1.7±0.2	1.5±0.4	2.1 ±0.5	1.9±0.2	-	2.3+0.2

$TOF_t = mol_{H_2\ produced} / [mol_{cat_t} \times$ reaction time (min)], where mol_{cat_t} is the mole of the total atoms of the catalyst, calculated at 10% conversion of $B_2(OH)_4$ hydrolysis.

$TOF_s = mol_{H_2\ produced} / [mol_{cat_s} \times$ reaction time], where mol_{cat_s} the turnover mole of the surface atoms of the catalyst, calculated at 10% conversion of $B_2(OH)_4$ hydrolysis.

The unit of TOF_t and TOF_s is $mol_{H_2}\ mol_{cat}^{-1}\ min^{-1}$. R_{atom} is the radius of the atom. N_s and N are the numbers of surface atoms and total atoms of the catalyst, respectively. R_L/R_D is the light enhancement rate.

impact the catalytic $B_2(OH)_4$ hydrolysis as indicated by the XPS data (Figure 3) involving Au and Rh in the alloyed Au_4Rh_1 NZs that exhibit an upshift of binding energy compared to the monometallic Au and Rh NZs. [42]

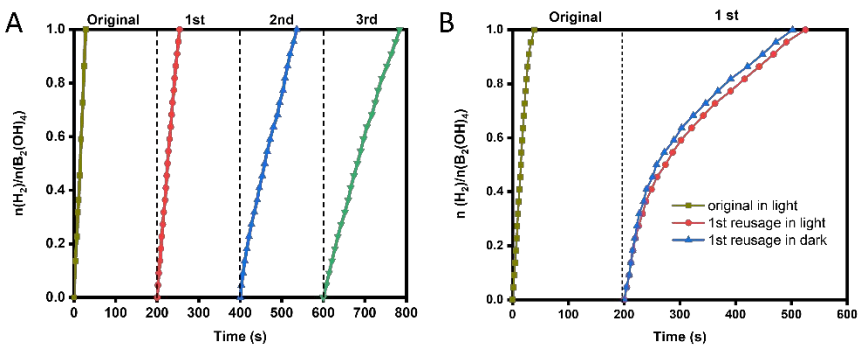

Figure 5. (A) Time plots of H_2 evolution for $B_2(OH)_4$ hydrolysis catalyzed by 1 mol % Au_4Rh_1NZ in the original, and 1st, 2nd and 3rd recycling tests in dark. (B) Time plots of H_2 evolution from $B_2(OH)_4$ hydrolysis catalyzed by 0.1 mol % Au_4Rh_1NZs under light (original) including 1st recycling under light and dark conditions. After photocatalysis, reused Au_4Rh_1NZs shows a TOF in dark or light of 1300 ± 200 $mol_{H_2}\ mol_{cat}^{-1}\ min^{-1}$)

3.3. Photocatalytic $B_2(OH)_4$ hydrolysis by the Au-Rh NZs

In order to explore the photocatalytic activity of the Au-Rh NZs, a low-power white-light LED was used to irradiate the reaction medium. Such a low-intensity light should avoid the participation of a significant photothermal effect (*vide infra*). As shown in Figure 6 and S16, the alloyed Au-Rh NZ clearly exhibits light-accelerated H_2 production, whereas the catalytic activities of the monometallic Au NZ and Rh NZ do not show any observable light-induced enhancement (Figure S 19). Besides, the Au_4Rh_1 NZ possess the highest TOF_s value in both dark and light conditions, as a result of the cumulative effect of synergy in the dark and light-induced enhancement. In order to further investigate the efficiency of light irradiation, the light-enhancement rate (R_L / R_D) is introduced here, defined by simply dividing the TOF_s value of the catalyst under visible light (R_L) by that enhancement. The R_L / R_D value is 1.2 for the most effective nanocatalyst, Au_4Rh_1 NZ. Under dark conditions (R_D). [43]

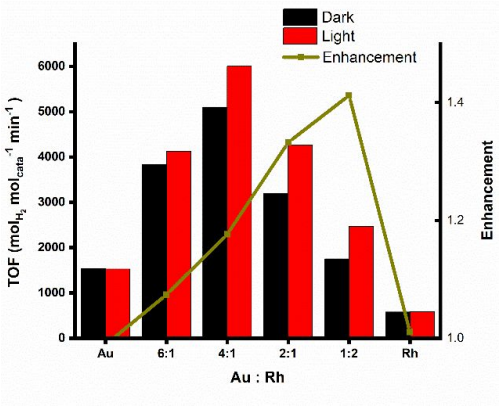

Figure 6. TOF_s value and enhancement rate (R_L/R_D) of $B_2(OH)_4$ hydrolysis photocatalyzed by 0.1 mol % Au-Rh NPs with various Au/Rh molar ratios at 25± 1˚C.

Many efforts have been devoted to the explanations of the photocatalysis mechanisms in the literature. For plasmonic metal NPs of Au and Ag, the surface plasmon resonance (SPR) effect is supposed to be the main factor responsible for the photocatalytic activity. [22, 24-26] Besides, it has been suggested that the photothermal effect is also involved in the light enhancement. [44] As the Au_1Rh_2 NZ exhibited the highest light-induced enhancement (Figure 6 and Table 1), it was selected for photocatalytic investigations. In order to search any photothermal effect, the temperature of the Au_1Rh_2 NZ catalyst was monitored during the light irradiation period. Specifically, the temperature change was recorded by a thermometer that was inserted in a sealed vial containing 4 ml catalyst under light illumination. The results (Figure S 17B) indicate that there is only 1.6 ºC temperature increase during 10 minutes of visible-light illumination, which shows only modest heat generation under such light irradiation under these conditions. Aiming at this clarification, the catalytic reaction was carried out, when the reaction vial was covered by tin foil, but

still exposed to light illumination. In this case, the catalytic system was still influenced by the light-induced heating, but there was no visible-light available for SPR-related acceleration. The results shown in Figure S 18A reveal that there is no significant catalytic efficiency variation between dark and tin foil-covered situations. Although there is heat release under light irradiation, the heating scale is negligible, because the catalytic reaction finishes within 3 min for Au_1Rh_2 NZs, which can only cause ~0.5˚C temperature increase under this light irradiation (Figure S 17B). The time plot in Figure S16D shows that H_2 generation in dark at 28˚C is less efficient than that in light at 25 ˚C. Besides, the temperature change of the catalytic reaction in light underwent almost the same route as that under dark conditions (Figure S 18B). All these results reveal that the photothermal effect in only an extremely minor component, if any, of the reason for the light-induced acceleration.

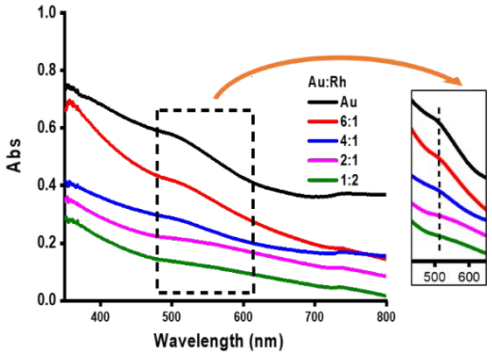

Figure 7. UV-vis. spectra of Au and Au-Rh NZs

On the other hand, the intrinsic plasmonic property of the prepared Au-Rh NPs is shown in Figure 7. Au NZ and Au-Rh NZ show a wide plasmon band around 500-540 nm, and the Au plasmonic absorption weakens as the percentage of Rh increases. This is ascribed to the shielding of the plasmon excitation of Au by Rh in the outer surface of the NP. [45,46] Previous studies have demonstrated that the integration of a plasmonic metal, such as Cu, Au, or Ag, and a catalytically active noble metal (e.g., Rh, Ru, Pd, or Pt) in a bimetallic system could be attributed to photocatalytic chemical transformations. [26] For instance, Ye et al reported a Rh-Au- $SrTiO_3$ photocatalyst for the synthesis of syngas using the CO_2 and H_2O under visible-light illumination. [47]

In the presence of light, the coherent electron oscillation of plasmonic Au nonradiative dephase results in the generation of hot electron carriers owing to the SPR effect. [24] Subsequently, giving a lower work function of Au (4.45 eV) than that of Rh (5.0 eV), [48] the active hot electrons resulting from the SPR of Au are driven to migrate to Rh sites. This equilibrates the Fermi level of a Au/Rh alloy within a few fs, causing an electron transfer from Au to Rh. The resulting enrichment of the Rh site favors oxidative addition cleavage

of a water O-H bond that is involved in the rate-determining step (*vide infra*). Therefore, the catalytic efficiency of $B_2(OH)_4$ hydrolysis is enhanced under light illumination. [43] Besides, the recyclability of Au_1Rh_2 NZ after photocatalysis is investigated. As shown in Figure 5B, after photocatalysis, reused Au_4Rh_1NZs shows a TOF in dark and light of 1300 ± 200 $mol_{H_2}\ mol_{cat}^{-1}\ min^{-1}$). There is almost no light-induced enhancement after photocatalysis for Au_1Rh_2NZs, probably indicating an atomic rearrangement of Au and Rh in the alloy, [49] which need further investigation.

In order to verify the role of the SPR in photocatalysis, lights with wavelengths of 520 nm and 450 nm were employed to conduct catalytic $B_2(OH)_4$ hydrolysis. Photon fluxes at different wavelength are calculated here for the analysis of photons on photocatalysis. [50] The result shown in Figure S24 indicates that 520 nm, which is near the SPR peak of Au/Rh NZs, is more efficient than 450 nm irradiation as indicated by the TOF_s comparison. On the other hand, photon flux, calculated following a standard ferrioxalate actinometry, [51] reveals that 450 nm irradiation (2.92×10^{-9} einsteins.s^{-1}) possesses a higher photon flux than 520 nm (2.34×10^{-9} einsteins·s^{-1}). This result indicates that irradiation by more photons does not necessarily lead to an increased efficiency, because it is selectively the light corresponding to the surface plasmon band of Au/Rh NZs that provides enhanced catalytic efficiency. [52]

In conclusion, Au_4Rh_1 NZ is the best nanocatalyst for this reaction both in the dark and under light illumination while Au_1Rh_2 NZs exhibit the highest light enhancement rate among a series of Au-Rh NZs. This result indicates the great significance of the metal proportions in an alloy and also demonstrates that Au is beneficial to this catalytic reaction in two cumulative ways: volcano-type synergy in dark and plasmonic effect under light illumination.

3.4. Kinetic study

In order to gain in-depth understanding of $B_2(OH)_4$ hydrolysis catalyzed by the Au-Rh NZs, the kinetics with Au_4Rh_1 NZ, the best catalyst in term of TOF_s, was investigated for catalytic H_2 generation under various catalysts, $B_2(OH)_4$ concentration and temperatures.

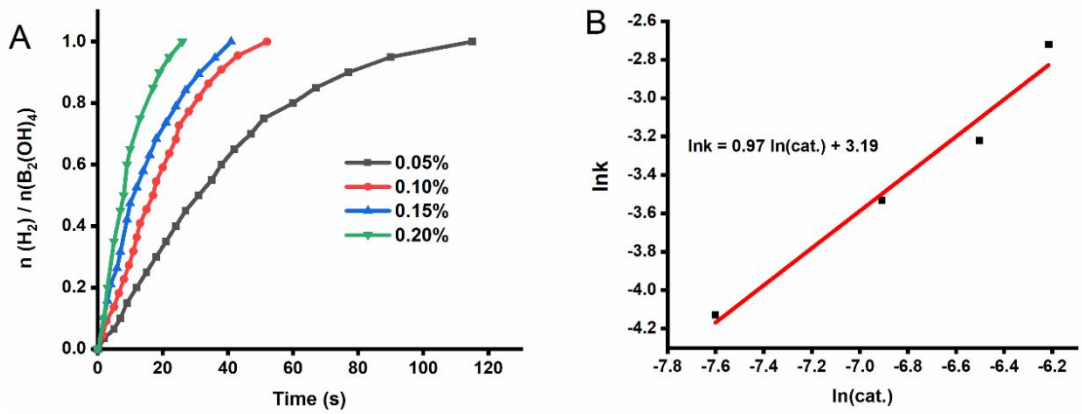

Figure 8. (A) Time plots of H_2 generation in the hydrolysis of $B_2(OH)_4$ catalyzed by various concentration of Au_4Rh_1 NZ catalyst in dark. (B) Plot of H_2 evolution rate vs. catalyst concentration ($R^2 = 0.96$).

Figure 8A shows the time plot of H_2 generation catalyzed by 0.05 mol %-0.2 mol % Au_4Rh_1 NZ at 25 ± 1 ºC. The hydrogen evolution exhibited a linear increase with respect to reaction time in the initial period. Based on the slope of the fitted linear portions of the plots, all the reaction rate constants (k) were calculated, providing the plot of the logarithm of H_2 evolution vs. Au_4Rh_1 NZ concentration in Figure 8B. The slope of the logarithmic plot was 0.97, indicating that the $B_2(OH)_4$ hydrolysis reaction is first order with respect to the catalyst concentration. [10]

The time plot of H_2 evolution at different concentrations of $B_2(OH)_4$ is shown in Figure 9A. The slope of the logarithmic plot of H_2 evolution vs. $B_2(OH)_4$ amount in Figure 9B is 0.107, demonstrating that H_2 generation closely follows zero-order kinetics in $B_2(OH)_4$ amount.

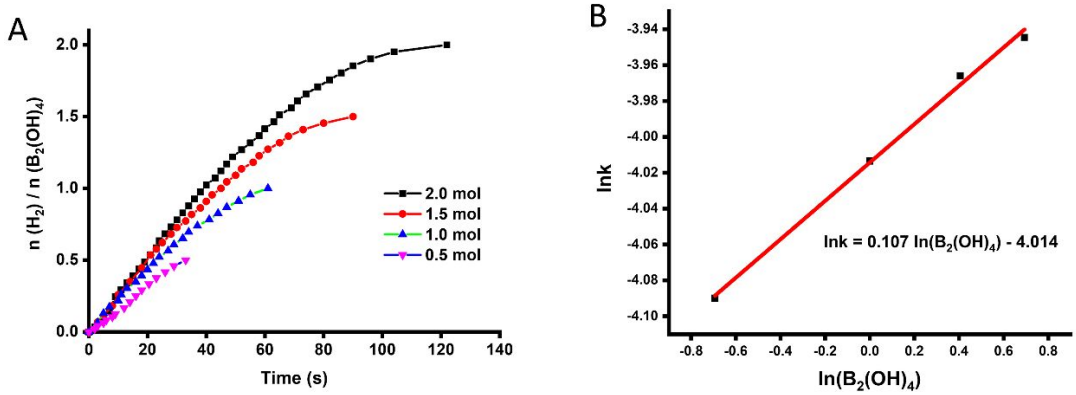

Figure 9. (A) Time plots of H_2 generation catalyzed by 0.1 mol % Au_4Rh_1 NZs with various $B_2(OH)_4$ amounts in the dark. (B) Plot of H_2 evolution rate vs. $B_2(OH)_4$ amount ($R^2 = 0.99$).

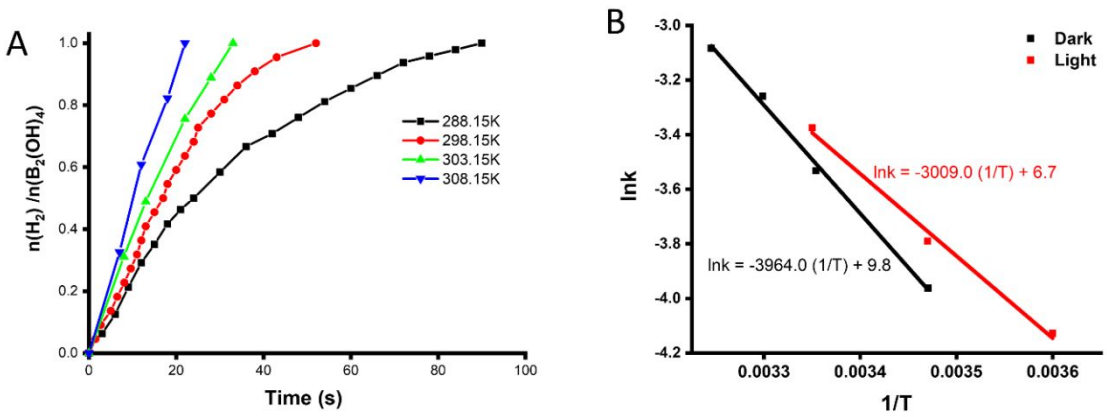

Figure 10. (A) Time plots of H_2 generation in the hydrolysis of $B_2(OH)_4$ catalyzed by 0.1 mol % Au_4Rh_1 NZs at various temperatures in the dark. (B) Arrhenius plots in the dark ($R^2 = 0.99$) and light ($R^2 = 0.98$) according to H_2 generation vs. time at different temperatures.

The time dependence of H_2 evolution catalyzed by 0.1 mol % Au_4Rh_1 NZ at different temperatures is illustrated in Figure 10A. As the reaction rate constant k is related to the activation energy (E_a) by the Arrhenius equation, [33] the Arrhenius plots of ln k vs. 1/T (Figure 10B) is depicted in accordance with the fitted linear parts of the plots in Figure 10A. The activation energy (E_a) is calculated to be 32.9 ± 1.4 kJ/mol in the dark and 25.0 ± 2.0 kJ/mol with visible light irradiation according to the Arrhenius equation (Equation S1). The reduced activation energy in light illumination may also be an indicator of the SPR-induced catalytic enhancement of H_2 evolution.

3.5. Mechanistic study

In order to confirm the hydrogen source of the produced H_2 gas, D_2O was used instead of H_2O as solvent in the hydrolysis of $B_2(OH)_4$ catalyzed by Au_4Rh_1. As shown in Figure 11, the catalysis in mixture dissolved in D_2O exhibits a lower slope in the time plot of H_2 generation, exhibiting a k_H/k_D value of 2.52 in dark. This result indicates a kinetic isotope effect (KIE) [11] showing that the cleavage of an O-H bond in water is involved in the rate-determining step of the $B_2(OH)_4$ hydrolysis process. The low KIE value is the result of a concerted process involving the O-H oxidative addition. Besides, the k_H/k_D value obtained upon light irradiation is 2.94 (Figure 11), higher than that in dark, which shows the increased role of O-H oxidative addition in the rate-limiting step compared to that upon reaction in the dark. This is in agreement with the electronic enrichment of the Rh site facilitating this O-H oxidative addition step.

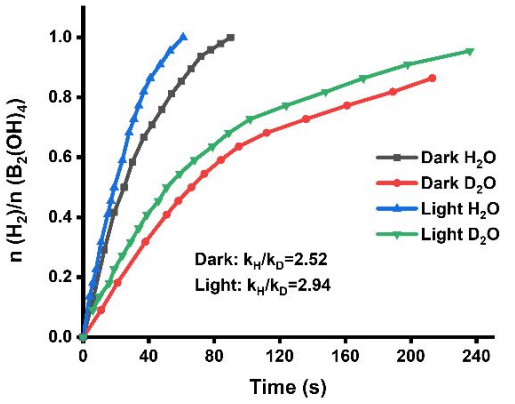

Figure 11. Time plot of hydrogen evolution catalyzed by 0.1 mol % Au_4Rh_1NPs in H_2O and D_2O in dark and light at 15 ±1˚C.

Successive reactions, in which the hydrolysis of $B_2(OH)_4$ and the hydrogenation of styrene utilizing the H_2 gas produced in the former step, were conducted in the same system. These experiments were then carried out in order to investigate the fate of the deuterium atoms. D_2 gas evolution occurred upon hydrolysis of $B_2(OH)_4$ catalyzed by Au_4Rh_1 NZ in D_2O in the left tube, meanwhile this gas was directed to the right tube to initiate the hydrogenation of styrene in CD_3OD in the presence of commercial Pd/C at room temperature (Figure S21). Hydrogenation of styrene occurs in methanol, while the nanocatalyst was in aqueous solution. The solid heterogeneous Pd/C hydrogenation catalyst was employed in the right tube. The product in the right tube was collected 24 h later, for analysis by ^{1}H NMR spectroscopy and gas chromatography–mass spectrometry. In the ^{1}H NMR spectra (Figure S22), a cluster of peaks at 7.11-7.28 ppm with 5-H integration reflects the existence of aromatic H atoms. No signals appear at 5~7ppm, indicating 100% conversion of styrene to deuterated ethylbenzene. Compared to normal ethylbenzene, reduced integration values of the peaks at 2.6 and 1.22-1.17 ppm were observed, showing deuteration of ethylbenzene in the right tube. Besides, in the mass spectrum (Figure S23), there were three peaks at around 107, 108 and 109 m/z corresponding to substitution of one, two and three H atom by D atoms in deuterated ethylbenzene. The mass spectrum of deuterated ethylbenzene contains not only the peak corresponding to bis-deuterated ethylbenzene as expected, but also minor peaks corresponding to mono- and tris-deuterated ethylbenzene. The presence of these odd numbers of D atoms in the ethylbenzene product is due to the stability of the styryl radical intermediate Ph-CH·-CH_3 (or deuterated analogues) that can exchange H (or D) atoms with the Pd_n-H or Pd_n-D catalytic species, Pd_n-H species being formed by reaction of partly deuterated ethylbenzene with the Pd_n catalyst, and Pd-D by oxidative addition of D_2 on Pd_n (**SI 3.4**). The formula found is Ph-$CH_{0.08}D_{1.92}$-$CH_{2.71}D_{0.29}$, in which the total number of D atoms in the deuterated ethylbenzene obtained is 2.2 ± 0.2 for 2 D expected. Between

$B_2(OH)_4$ and D_2O, fast H/D exchange occurs between these two oxo-acids, but D_2O is in such a very large molar excess (450/1), so that the final proportion of H atoms in D_2 formed is negligeable.

All these results confirm those obtained by direct alkene hydrogenation [5] and verify that both hydrogen atoms of the produced hydrogen gas are originated from water. Accordingly, a mechanism of $B_2(OH)_4$ hydrolysis catalyzed by Au-Rh NZs is proposed

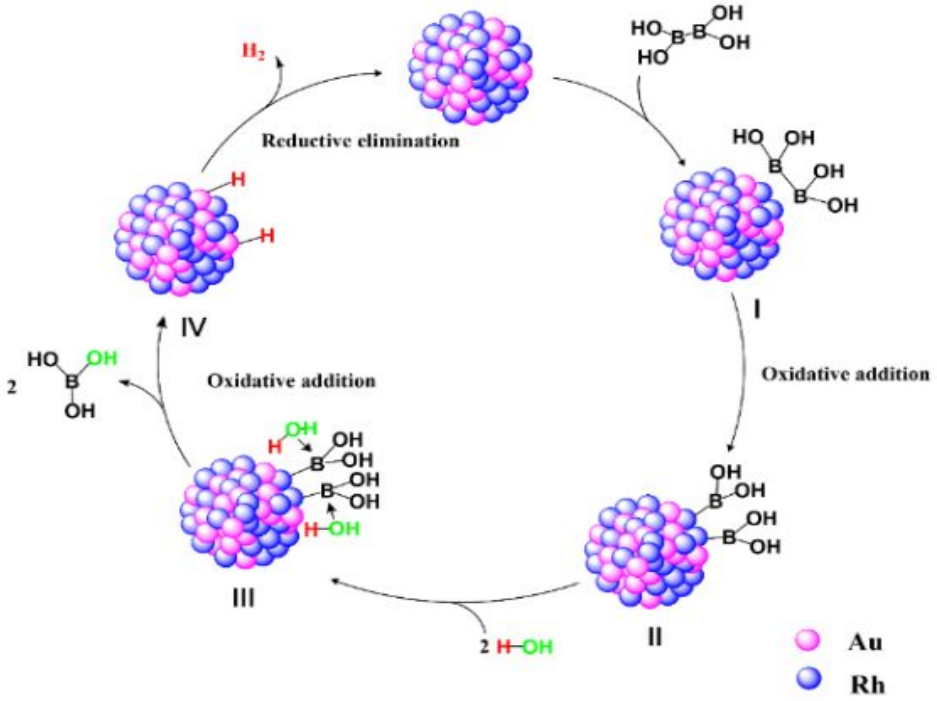

Figure 12. Schematic illustration of the confirmed mechanism of the $B_2(OH)_4$ dehydrogenation catalyzed by the nanozyme catalysts Au-RhNZ @click dendrimer.

here (Figure 12). In the first step of the catalytic cycle, $B_2(OH)_4$ is adsorbed onto the catalyst surface to give the intermediate Ⅰ. Subsequently, the intermediate Ⅱ is obtained following oxidative addition of the B-B bond onto the metal surface. [5,9] Owing to the electron-deficiency of the Lewis-acidic B-containing species, two H_2O molecules obviously act as Lewis base to coordinate two boron atoms giving the intermediate Ⅲ. At this point, the oxidative addition of an O-H bond of H_2O is facilitated by the initial H_2O coordination to the boron atoms bringing these O-H bonds close to the catalyst surface. The result is the formation of the two NP-H bonds, as shown by the D_2O experiments, and the release of 2 $B(OH)_3$ whose formation was demonstrated earlier, [9] giving intermediate Ⅳ. Finally, the generated hydride-[M]-hydride intermediate Ⅳ produces H_2 upon reductive elimination. [53]

As indicated in the introduction, there are similarities between this mechanism and that of hydrogenase including, first, the origin (water) of both atoms forming H_2. Then, mechanistically, in hydrogenase, two water protons are successively transferred to heteroatoms of the ligand bound to the metal site together with electrons, before their transfer to the metal site, followed by reductive elimination to yield H_2. Here, the metal site of the NZs is played by the bimetallic NP. The two water protons are transferred via the two boron species before subsequent transfer to the NP, which is also followed by reductive elimination like in the hydrogenase enzyme. These mechanistic features are in sharp contrast with those involved in borohydride or ammonia-borane hydrolysis, whereby first a hydride is transferred from the borane precursor followed by proton transfer from water in the second step. The beneficial use of visible light for the NZs is compatible with the same $B_2(OH)_4$ hydrolysis mechanism, just clearly accelerating the last step, reductive elimination, by increasing the electron density on Rh through electronic donation upon transfer from the plasmonic metal, Au.

4. Conclusion

A series of alloyed Au-Rh NP catalysts supported and encapsulated by a "click" dendrimer (called nanozymes, NZs) were prepared, extensively characterized, then utilized for H_2 production upon $B_2(OH)_4$ hydrolysis and convenient hydrogenation reactions with produced H_2. These Au-Rh NZs with different molar ratios of the two metals in the alloys were shown to exhibit different catalytic efficiencies, the optimized composition being Au_4Rh_1 with sharp volcano-type synergies of 3.4-fold and 8.9-fold increased TOF_s compared to the monometallic Au and Rh NZs, respectively. The plasmonic Au-Rh NZs also exhibit remarkable additional enhancement of catalytic activity under visible-light illumination provoking what appears to be hot electron injection from plasmonic Au to Rh-adsorbed substrates at the nearby Rh atom and giving the highest light enhancement rate of 1.4 for Au_1Rh_2 NZ. Although the synergistic sharp volcano-type enhancement in the dark and light-induced enhancements show their maxima for distinct proportions of the two metals in the alloy, the two effects are cumulative, and the maximum combined enhancement effect is obtained for the Au_4Rh_1 NZ. In the alloy, Au plays both roles of most efficient partner in the synergistic volcano-type effect and source of plasmonic charge

transfer, which explains why the percentage of the part of Au atoms among the two metals is much larger than the Rh part in the optimized catalyst, Au_4Rh_1 NZ. Kinetic and isotopic studies along with successive reactions confirm the mechanism of $B_2(OH)_4$ hydrolysis, indicating that both hydrogen atoms of formed H_2 are coming from water (contrary to ammonia borane), like with hydrogenase. This work illustrates a rational design of the function of plasmonic metal in light-accelerated bimetallic photo-catalysis and a facile strategy for H_2 (or D_2) evolution from H_2O (resp. D_2O) based on $B_2(OH)_4$ hydrolysis together with application of H_2 (resp. D_2) formed.

ASSOCIATED CONTENT

4.Supporting Information.

Materials and methods, nanomaterials characterizations, and kinetics and compared performances of Au-Rh nanocatalyzed in $B_2(OH)_4$ hydrolysis.

AUTHOR INFORMATION

5. Corresponding Author

Didier Astruc - ISM, UMR CNRS N° 5255, Univ. Bordeaux, 33405 Talence Cedex, France; orcid.org/000-0001-6446-8751; E-mail: didier.astruc@u-bordeaux.fr

6. Authors

Qiuxia Zhao- LCC, CNRS & University of Toulouse III, 205 Route de Narbonne, 31077 Toulouse Cedex, France. ISM, UMR CNRS N° 5255, Univ. Bordeaux, 33405 Talence Cedex, France; https://orcid.org/0000-0002-5618-1379; E-mail: zqx52028@gmail.com

Naixin Kang- ISM, UMR CNRS N° 5255, Univ. Bordeaux, 33405 Talence Cedex, France; https://orcid.org/0000-0001-8364-4343; Email: knxcarnation@foxmail.com

Marta Martinez Moro - Soft Matter Nanotechnology Lab, CIC biomaGUNE, Paseo Miramón 182. 20014. Donostia-San Sebastián, Gipuzkoa, Spain ; https://orcid.org/0000-0001-9380-9973; E-mail : mmartinez@cicbiomagune.es

Eduardo Guisasola Cal - Soft Matter Nanotechnology Lab, CIC biomaGUNE, Paseo Miramón 182. 20014. Donostia-San Sebastián, Gipuzkoa, Spain; https://orcid.org/0000-0002-2549-1745

E-mail : eguisasola@cicbiomagune.es

Sergio Moya - Soft Matter Nanotechnology Lab, CIC biomaGUNE, Paseo Miramón 182. 20014. Donostia-San Sebastián, Gipuzkoa, Spain ; https://orcid.org/0000-0002-7174-1960. Email : smoya@cicbiomagune.es

Emerson Coy- NanoBioMedical Centre, Adam Mickiewicz University in Poznań, Wszechnicy Piastowskiej 3, 61-614 Poznań, Poland; https://orcid.org/0000-0002-4149-9720.

E-mail : coyeme@amu.edu.pl

Lionel Salmon- LCC, CNRS & University of Toulouse III, 205 Route de Narbonne, 31077 Toulouse Cedex, France ; https://orcid.org/0000-0002-8064-8960. E-mail : lionel.salmon@lcc-toulouse.fr

E-mail : lionel.salmon@lcc-toulouse.fr

Xiang Liu- College of Materials and Chemical Engineering, Key Laboratory of Inorganic Nonmetallic Crystalline and Energy Conversion Materials, China Three Gorges University, Yichang 443002, Hubei, China; https://orcid.org/0000-0002-0213-637X; E-mail : xiang.liu@ctgu.edu.cn

Notes

The authors declare no conflict of interest.

ACKNOWLEDGMENT

Helpful comments from Dr Desire di Silvio, (CIC biomaGUNE, San Sebastian) and financial support from the China Scholarship Council (CSC, PhD grants to Q.Z. and N.K.), the National Science Centre of Poland under the program OPUS (E.C.: 2019/35/B/ST5/00248 and S.M.: 2019/33/B/ST5/01495), MAT2017-88752-R (S.M.), the National Natural Science Foundation of China (21805166), the 111 Project (D20015) (X. L.), the Centre National de la Recherche Scientifique (CNRS) and the University of Bordeaux are gratefully acknowledged.

References

1. Huang, Y.; Re, J.; Qu, X. Nanozymes: Classification, Catalytic Mechanisms, Activity Regulation, and Applications. *Chem. Rev*. **2019**, *119*, 4357-4412.

2. Astruc, D. Introduction: Nanoparticles in Catalysis. *Chem. Rev*. **2020**, *120*, 461-463.
3. Lubitz, W.; Ogata, H,; Rudiger, O.; Reijerse, E. Hydrogenases. *Chem. Rev*. **2014**, *114*, 4081-4148.
4. Amaro-Gahete, J.; Pavliuk, M. V.; Tian, H. N.; Esquivel, D.; Romero-Salguero, F. J.; Ott, S. Catalytic Systems mimicking the [Fe-Fe]-hydrogenase active site for visible-light hydrogen production. *Coord. Chem. Rev*. **2021**, *448*, 214172.
5. Cummings, S. P.; Le, T. N.; Fernandez, G. E.; Quiambao, L. G.; Stokes, B. J. Tetrahydroxydiboron-Mediated Palladium-Catalyzed Transfer Hydrogenation and Deuteriation of Alkenes and Alkynes Using Water as the Stoichiometric H or D Atom Donor. *J. Am. Chem. Soc.* **2016,** *138*, 6107-6110.
6. Zhou, Y. Huang, J. Shen, X. Liu, Pd/C-Catalyzed H_2 Evolution from Tetrahydroxydiboron Hydrolysis, Catal. Letters **2021**, *151*, 3004-3010.
7. Jang, M.; Lim, T.; Park, B. Y.; Han, M. S. Metal-Free, Rapid, and Highly Chemoselective Reduction of Aromatic Nitro Compounds at Room Temperature, *J. Org. Chem*. **2022**, *87*, 910-919.
8. Chen, W.; Shen, J.; Huang, Y.; Liu, X.; Astruc, D. Catalyzed Hydrolysis of Tetrahydroxydiboron by Graphene Quantum Dot-Stabilized Transition-Metal Nanoparticles for Hydrogen Evolution. *ACS Sustain. Chem. Eng.* **2020,** *8*, 7513-7522.
9. Wang, D.; Astruc, D. The Golden Age of Transfer Hydrogenation. *Chem. Rev.* **2015,** *115*, 6621-6686;
10. Fu, F.; Wang, C.; Wang, Q.; Martinez-Villacorta, A. M.; Escobar, A.; Chong, H.; Wang, X.; Moya, S.; Salmon, L.; Fouquet, E.; Ruiz, J.; Astruc, D. Highly Selective and Sharp Volcano-type Synergistic Ni_2Pt@ZIF-8-Catalyzed Hydrogen Evolution from Ammonia Borane Hydrolysis. *J. Am. Chem. Soc.* **2018**, *140*, 10034-10042.
11. Gómez-Gallego, M.; Sierra, M. A. Kinetic Isotope Effects in the Study of Organometallic Reaction Mechanisms. *Chem. Rev.* **2011,** *111*, 4857-4963.
12. Atzrodt, J.; Derdau, V. Pd- and Pt-catalyzed H/D exchange methods and their application for internal MS standard preparation from a Sanofi-Aventis perspective. *J. Labelled Compd. Radiopharm.* **2010,** *53*, 674-685.
13. Sloane, S. E.; Reyes, A.; Vang, Z. P.; Li, L.; Behlow, K. T.; Clark, J. R. Copper-Catalyzed Formal Transfer Hydrogenation/Deuteration of Aryl Alkynes. *Org. Lett.* **2020,** *22*, 9139-9144.
14. Chu, S.; Cui, Y.; Liu, N. The path towards sustainable energy, *Nat. Mater.* **2017**, *16,* 16-20.
15. Zhu, Y.; Ouyang, L.; Zhong, H.; Liu, J.; Wang, H.; Shao, H.; Huang, Z.; Zhu, M. Closing the Loop for Hydrogen Storage: Facile Regeneration of $NaBH_4$ from its Hydrolytic Product, *Angew. Chem. Int. Ed.* **2020**, *59,* 8623-8629.
16. Liu, C. C.; Gong, T.; Zhang, J.; Zheng, X. R.; Mao, J.; Liu, H.; Li, Y.; Hao, Q. Y., Engineering Ni_2P-$NiSe_2$ heterostructure interface for highly efficient alkaline hydrogen evolution. *Appl. Catal. B-Environ.* **2020,** *262*.
17. Wang, H. F.; Chen, L. Y.; Pang, H.; Kaskel, S.; Xu, Q., MOF-derived electrocatalysts for oxygen reduction, oxygen evolution and hydrogen evolution reactions. *Chem. Soc. Rev.* 2020, *49* (5), 1414-1448.
18. Lin, Y.; Sun, K. A.; Chen, X. M.; Chen, C.; Pan, Y.; Li, X. Y.; Zhang, J., High-precision regulation synthesis of Fe-doped Co_2P nanorod bundles as efficient electrocatalysts for hydrogen evolution in all-pH range and seawater. *Journal of Energy Chemistry* **2021,** *55*, 92-101.
19. Zhu, J.; Hu, L. S.; Zhao, P. X.; Lee, L. Y. S.; Wong, K. Y., Recent Advances in Electrocatalytic Hydrogen Evolution Using Nanoparticles. *Chem. Rev.* **2020,** *120* (2), 851-918.
20. Zaleska-Medynska, A.; Marchelek, M.; Diak, M.; Grabowska, E. Noble metal-based bimetallic nanoparticles: the effect of the structure on the optical, catalytic and photocatalytic properties. *Adv. Colloid Interface Sci.* **2016,** *229*, 80-107.
21. Gilroy, K. D.; Ruditskiy, A.; Peng, H.-C.; Qin, D.; Xia, Y. Bimetallic Nanocrystals: Syntheses, Properties, and Applications. *Chem. Rev.* **2016,** *116*, 10414-10472.

22. Wang, C.; Astruc, D. Nanogold plasmonic photocatalysis for organic synthesis and clean energy conversion. *Chem. Soc. Rev.* **2014**, *43*, 7188-7216.
23. Daniel, M-C.; Astruc, D., Gold Nanoparticles: Assembly, Supramolecular Chemistry, Quantum-size Related Properties, and Applications towards Biology, Catalysis and Nanotechnology, *Chem. Rev*. **2004***, 104*, 293-346.
24. Zada, A.; Muhammad, P.; Ahmad, W.; Hussain, Z.; Ali, S.; Khan, M.; Khan, Q.; Maqbool, M. Surface Plasmonic-Assisted Photocatalysis and Optoelectronic Devices with Noble Metal Nanocrystals: Design, Synthesis, and Applications. *Adv. Funct. Mater.* **2019,** *30*, 1906744.
25. Gelle, A.; Jin, T.; de la Garza, L.; Price, G. D.; Besteiro, L. V.; Moores, A. Applications of Plasmon-Enhanced Nanocatalysis to Organic Transformations. *Chem. Rev*. **2020**, *120*, 986-1041.
26. Verma, P.; Kuwahara, Y.; Mori, K.; Yamashita, H. Pd/Ag and Pd/Au bimetallic nanocatalysts on mesoporous silica for plasmon-mediated enhanced catalytic activity under visible light irradiation. *J. Mater. Chem. A* **2016**, *4*, 10142-10150.
27. J. S. Chahal, O. F. Khan, C. L. Cooper, J. S. McPartlan, J. K. Tsosie, L. D. Tilley, S. M. Sidik, S. Lourido, R. Langer, S. Bavari, H. Ploegh and D. G. Anderson. Dendrimer-RNA Nanoparticles Generate Protective Immunity Against Iethal Ebola, H1N1 Influenza, and Toxoplasma Gondii Challenges with a Single Dose, *Proc. Natl. Acad. Sci. USA*, **2016**, *113*, E4133–4142.
28. R. W. Scott, O. M. Wilson and R. M. Crooks, Synthesis, Characterization, and Applications of Dendrimer-Encapsulated Nanoparticles, *J. Phys. Chem. B*, **2005**, *109*, 692-704.
29. V. S. Myers, M. G. Weir, E. V. Carino, D. F. Yancey S. Pande and R. M. Crooks. Dendrimer-encapsulated Nanoparticles : New Synthetic and Characterization Methods and Catalytic Applications, *Chem. Sci*., **2011**, *2*, 1632-1646
30. Astruc, D.; Boisselier, E.; Ornelas, C. Dendrimers Designed for Functions: From Physical, Photophysical, and Supramolecular Properties to Applications in Sensing, Catalysis, Molecular Electronics, Photonics, and Nanomedicine. *Chem. Rev.* **2010**, *110*, 1857-1959.
31. Wang, C.; Ikhlef, D.; Kahlal, S.; Saillard, J.-Y.; Astruc, D. Metal-Catalyzed Azide-Alkyne "Click" Reactions: Mechanistic Overview and Recent Trends. *Coord. Chem. Rev.* **2016**, *316*, 1-20.
32. Astruc, D.; Heuzé, K.; Gatard, S.; Méry, D.; Nlate, S.; Plault, L. Metallodendritic Catalysis for Redox and Carbon-Carbon Bond Formation Reactions: A Step towards Green Chemistry. *Adv. Synth. Catal*. **2005**, *347*, 329-338.
33. Wang, Q.; Fu, F.; Yang, S.; Martinez Moro, M.; Ramirez, M. d. l. A.; Moya, S.; Salmon, L.; Ruiz, J.; Astruc, D. Dramatic Synergy in CoPt Nanocatalysts Stabilized by "Click" Dendrimers for Evolution of Hydrogen from Hydrolysis of Ammonia Borane. *ACS Catal*. **2019**, *9*, 1110-1119.
34. Bian, T.; Xiao, B.; Sun, B.; Huang, L.; Su, S.; Jiang, Y.; Xiao, J.; Yuan, A.; Zhang, H.; Yang, D. Local epitaxial growth of Au-Rh core-shell star-shaped decahedra: A case for studying electronic and ensemble effects in hydrogen evolution reaction. *Appl. Catal. B* **2020,** *263*, 118255.
35. Kang, Y. Q.; Xue, Q.; Peng, R. L.; Jin, P. J.; Zeng, J. H.; Jiang, J. X.; Chen, Y. Bimetallic AuRh nanodendrites consisting of Au icosahedron cores and atomically ultrathin Rh nanoplate shells: synthesis and light-enhanced catalytic activity. *NPG Asia Mater.* **2017,** *9*.
36. Ding, J.; Li, X.; Chen, L.; Zhang, X.; Tian, X. Photocatalytic hydrogen production over plasmonic AuCu/$CaIn_2S_4$ composites with different AuCu atomic arrangements. *Appl. Catal. B* **2018**, *224*, 322-329.
37. Saad, A.; Vard, C.; Abderrabba, M.; Chehimi, M. M. Triazole/Triazine-Functionalized Mesoporous Silica As a Hybrid Material Support for Palladium Nanocatalyst. *Langmuir* **2017,** *33*, 7137-7146.
38. Moulder, J.F.; Stickle, W.F.; Sobol, P.E.; Bomben, K.D. Handbook of X ray Photoelectron Spectroscopy, *Physical Electronics*, **1995**
39. Marcus, R. A. On the Theory of Oxidation-Reduction Reactions Involving Electron Transfer. I. *J. Chem. Phys.* **1956,** *24*, 966-978.

40. Tedsree, K.; Li, T.; Jones, S.; Chan, C. W.; Yu, K. M.; Bagot, P. A.; Marquis, E. A.; Smith, G. D.; Tsang, S. C. Hydrogen production from formic acid decomposition at room temperature using a Ag-Pd core-shell nanocatalyst. *Nat. Nanotechnol.* **2011,** *6*, 302-307.
41. Schüth, F.; Ward, M. D.; Buriak, J. M. Common Pitfalls of Catalysis Manuscripts Submitted to Chemistry of Materials. *Chem. Mater.* **2018,** *30*, 3599-3600.
42. Gao, F.; Goodman, D. W. Pd–Au bimetallic catalysts: understanding alloy effects from planar models and (supported) nanoparticles. *Chem. Soc. Rev.* **2012,** *41*, 8009-8020.
43. Verma, P.; Yuan, K.; Kuwahara, Y.; Mori, K.; Yamashita, H. Enhancement of plasmonic activity by Pt/Ag bimetallic nanocatalyst supported on mesoporous silica in the hydrogen production from hydrogen storage material. *Appl. Catal. B-Environ.* **2018,** *223*, 10-15.
44. Dubi, Y.; Un, I. W.; Sivan, Y. Thermal effects – an alternative mechanism for plasmon-assisted photocatalysis. *Chem. Sci.* **2020,** *11*, 5017-5027.
45. Yin, Z.; Wang, Y.; Song, C.; Zheng, L.; Ma, N.; Liu, X.; Li, S.; Lin, L.; Li, M.; Xu, Y.; Li, W.; Hu, G.; Fang, Z.; Ma, D. Hybrid Au–Ag Nanostructures for Enhanced Plasmon-Driven Catalytic Selective Hydrogenation through Visible Light Irradiation and Surface-Enhanced Raman Scattering. *J. Am. Chem. Soc.* **2018,** *140*, 864-867.
46. Ma, Y.; Li, W.; Cho, E. C.; Li, Z.; Yu, T.; Zeng, J.; Xie, Z.; Xia, Y. Au@Ag Core−Shell Nanocubes with Finely Tuned and Well-Controlled Sizes, Shell Thicknesses, and Optical Properties. *ACS Nano* **2010,** *4*, 6725-6734.
47. Li, D.; Ouyang, S.; Xu, H.; Lu, D.; Zhao, M.; Zhang, X.; Ye, J. Synergistic effect of Au and Rh on $SrTiO_3$ in significantly promoting visible-light-driven syngas production from CO_2 and H_2O. *Chem. Commun*. **2016**, *52*, 5989-5992.
48. Trasatti, S. Work function, electronegativity, and electrochemical behaviour of metals: II. Potentials of zero charge and "electrochemical" work functions. *J. Electroanal. Chem.* **1971**, *33*, 351-378.
49. Kang, N.; Wang, Q.; Djeda, R.; Wang, W.; Fu, F.; Moro, M. M.; Ramirez, M. d. l. A.; Moya, S.; Coy, E.; Salmon, L.; Pozzo, J.-L.; Astruc, D., Visible-Light Acceleration of H_2 Evolution from Aqueous Solutions of Inorganic Hydrides Catalyzed by Gold-Transition-Metal Nanoalloys. *ACS Appl. Mater. Interfaces* **2020,** *12* (48), 53816-53826.
50. Qureshi, M.; Takanabe, K., Insights on Measuring and Reporting Heterogeneous Photocatalysis: Efficiency Definitions and Setup Examples. *Chem. Mater.* **2017,** *29* (1), 158-167
51. Cornilleau, T.; Hermange, P.; Fouquet, E., Gold-catalysed cross-coupling between aryldiazonium salts and arylboronic acids: probing the usefulness of photoredox conditions. *Chem. Commun.* **2016,** *52* (65), 10040-10043.
52. Xu, P.; Lu, W.; Zhang, J.; Zhang, L., Efficient Hydrolysis of Ammonia Borane for Hydrogen Evolution Catalyzed by Plasmonic Ag@Pd Core–Shell Nanocubes. *ACS Sustain. Chem. Eng.* **2020,** *8* (33), 12366-12377.
53. Astruc, D. *Organometallic Chemistry and Catalysis*. Springer, Berlin, **2007**, pp 87-95.

TOC graphic

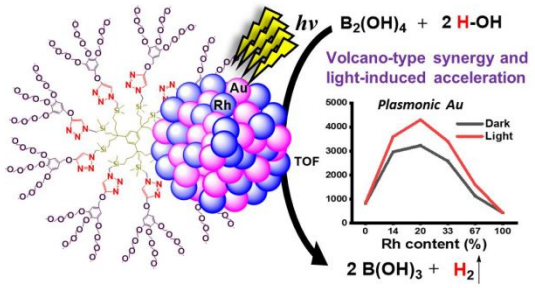
hν
Au
Rh
TOF
B2(OH)4 + 2 H-OH
Volcano-type synergy and light-induced acceleration
Plasmonic Au
Dark
Light
5000
4000
3000
2000
1000
0
0
14
20
33
67
100
Rh content (%)
2 B(OH)3 + H2